

## Feed-Horn Antenna for Enhanced Uncooled Infrared Sensor Using Novel UV Lithography, Plastic Micromachining and Mesh Structure Bonding

Jong-Yeon PARK, Kun-Tae KIM, Hyun-Joon SHIN, Sung MOON and James Jungho PAK<sup>1</sup>

Microsystems Research Center, Korea Institute of Science and Technology, P.O. BOX 131, Cheongryang, Seoul, Korea

<sup>1</sup>Department of Electrical Engineering, Korea University, Seoul 136-701, Korea

(Received October 21, 2003; accepted January 20, 2004; published June 9, 2004)

In this paper, we report a uncooled infrared sensor coupled with a 3-dimensional (3D) feed-horn shape micro-electro-mechanical system (MEMS) antenna using novel UV lithography technique for fabricating a 3D feed-horn-shaped mold array, obtaining parallel light using a mirror-reflected parallel-beam illuminator (MRPBI) system and plastic micromachining. The microassembly of infrared detector and 3D feed-horn-shaped antenna arrays is difficult using the conventional MEMS bonding process. To overcome limitation, the proposed novel 3D MEMS bonding technique is mesh structure bonding (MSB) using microchannels with micromolding in capillaries by polydimethylsiloxane (PDMS). The feasibility of fabricating both a 3D feed-horn MEMS antenna and a mold array was demonstrated. As a result, it seems possible to use a 3D feed-horn-shaped MEMS antenna to improve uncooled infrared sensor performance and applications to fabricate MEMS device.

[DOI: 10.1143/JJAP.43.3320]

KEYWORDS: 3D MEMS antenna, mesh structure bonding, mirror-reflected parallel-beam illuminator system, infrared sensor

### 1. Introduction

Recent advances in the micro-electro-mechanical systems (MEMS) industries have given rise to the advent of various MEMS fabrication techniques for fabricating microstructures from various materials.<sup>1–3</sup> There is also a need for complicated 3-dimensional microstructures with high aspect ratios for such applications as enhanced microbolometer-coupled 3D MEMS antenna arrays and enhanced optical efficiency TFT-LCDs and other display devices.<sup>4,5</sup> Figure 1 shows a schematic drawing of a 3D feed-horn MEMS antenna coupled with a microbolometer. Although the 3D feed-horn MEMS antenna structures have many advantages, it is difficult to fabricate them using conventional UV lithography techniques. In this paper, a novel method for realizing 3D feed-horn MEMS antenna arrays using a mirror-reflected parallel-beam illuminator (MRPBI) system is presented.

### 2. Concepts and Implementation of MRPBI System

The most difficult problem in the fabrication of high-aspect-ratio structures (HARS) and 3D feed-horn-shaped MEMS antenna arrays is how to achieve a parallel beam when using a UV lithography apparatus. UV light propagation longer than 6 m would be required for a 11.16 cm<sup>2</sup>

exposure area. According to the CODE V optical simulator, however, since a typical laboratory height is less than 6 m, it is almost impossible to set up the apparatus in a typical laboratory.<sup>6</sup>

As an alternative, reflecting light from several cold mirrors can generate a long propagation path when using UV light. Figures 2 and 3 show schematic drawings of the MRPBI system and the configuration of the MRPBI system, respectively.

A conventional UV lithography apparatus is required to expose the planar stage, but the MRPBI system exposure method is different. For fabrication of higher aspect-ratio 3D structure arrays, the stage has an *x*-*y*-*z* tilt 360° automatic rotation control and simultaneous exposure. Because more parallel UV light is available, the MRPBI system exposure area is smaller than that for conventional UV lithography.

A mask coupled with a wafer can be employed in a 2-way fixed vacuum, and the stage can be controlled to select hard contact, soft contact, and several other contact conditions. Figure 4 shows a photograph of the inside of the MRPBI system. Its rotational axis can be controlled two ways: manually and by computer using an RS-232C communication port. Thus, we can change two experiment parameters: the rotation time and the exposure time. The MRPBI's wavelength is 365 nm for a 1 kW SHP Hg lamp, and its

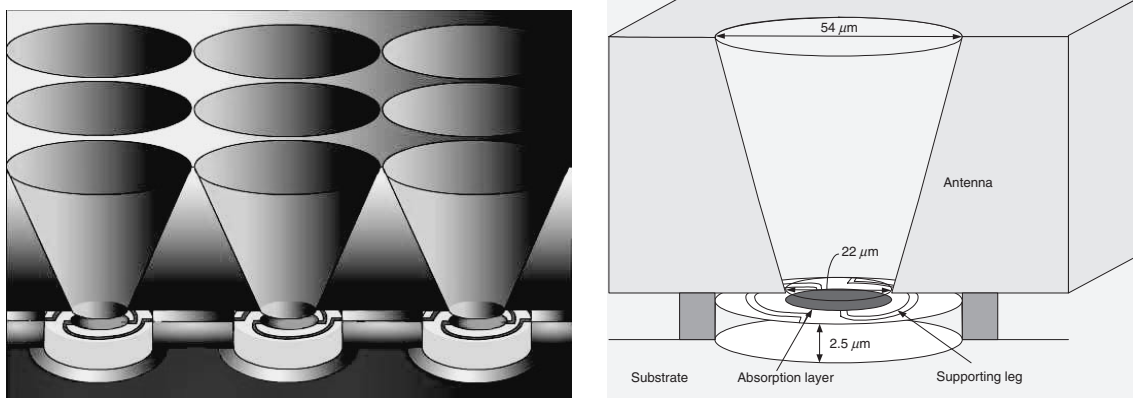


Fig. 1. Schematic drawing of a 3D feed-horn MEMS antenna coupled with a microbolometer.

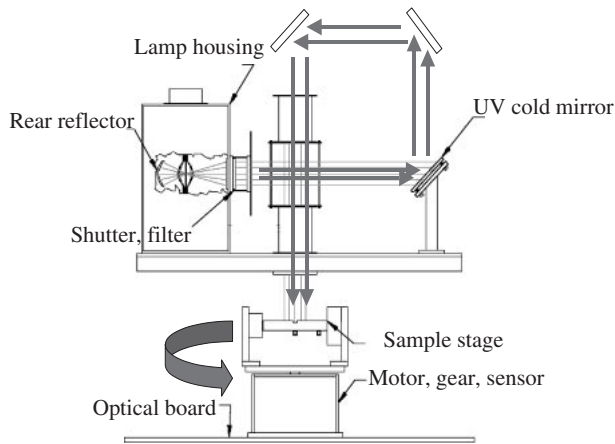


Fig. 2. Schematic drawing of the MRPBI system.

radiation intensity can be changed to a maximum of 10 mW/Cm<sup>2</sup>.

### 3. Optimal Design of 3D MEMS Antenna and Microbolometer

#### 3.1 Design of 3D MEMS antenna

The thermal or blackbody radiation emitted by all objects at a given temperature that generates infrared light becomes maximum in the wavelength range from 8 to 12 μm. Thus, we considered the 3D antenna dimensions in relation to the development of a new form of IR imaging array that uses 3D feed-horn MEMS antenna technology to couple the incident thermal radiation into an individual array element or pixel. The HFSS uses the following equations for the optimal design and simulation of a conical feed-horn antenna

$$D_c(dB) = 10 \log_{10} \left[ \varepsilon_{ap} \frac{4\pi}{\lambda^2} (\pi a)^2 \right]$$

$$= 10 \log_{10} \left( \frac{C}{\lambda} \right)^2 - L(s)$$

$$L(s) = -10 \log_{10}(\varepsilon_{ap})$$

$$\cong (0.8 - 1.71s + 26.25s^2 - 17.79s^3)$$

$$s = \frac{d_m^2}{8\lambda l}$$

Here,  $D_c$  is the directivity of the conical horn,  $a$  is the radius of the horn at the aperture,  $L(s)$  is the directivity loss of aperture efficiency,  $C$  is the aperture circumference,  $s$  is the maximum phase deviation, and  $\varepsilon_{ap}$  is the aperture efficiency. The following three equations are used for a feed-horn antenna

$$\frac{L}{\lambda} = \frac{0.3 \times \cos \theta}{1 - \cos \theta}$$

$$\frac{d_m}{\lambda} = \frac{0.6 \times \sin \theta \times \cos \theta}{1 - \cos \theta}$$

$$L = \frac{d_m}{2 \times \sin \theta}$$

Here,  $L$  is the feed-horn length and  $d_m$  is the feed-horn diameter.<sup>7)</sup>

Figures 5, 6, and 7 show the results of the 3D cylinder MEMS antenna simulation, the 3D conical horn MEMS antenna simulation, and the 3D feed-horn MEMS antenna simulation, respectively. Figures 5, 6, and 7 show scattered radiation patterns from the simulation results. They indicate



Fig. 4. Photograph of inside the MRPBI system.

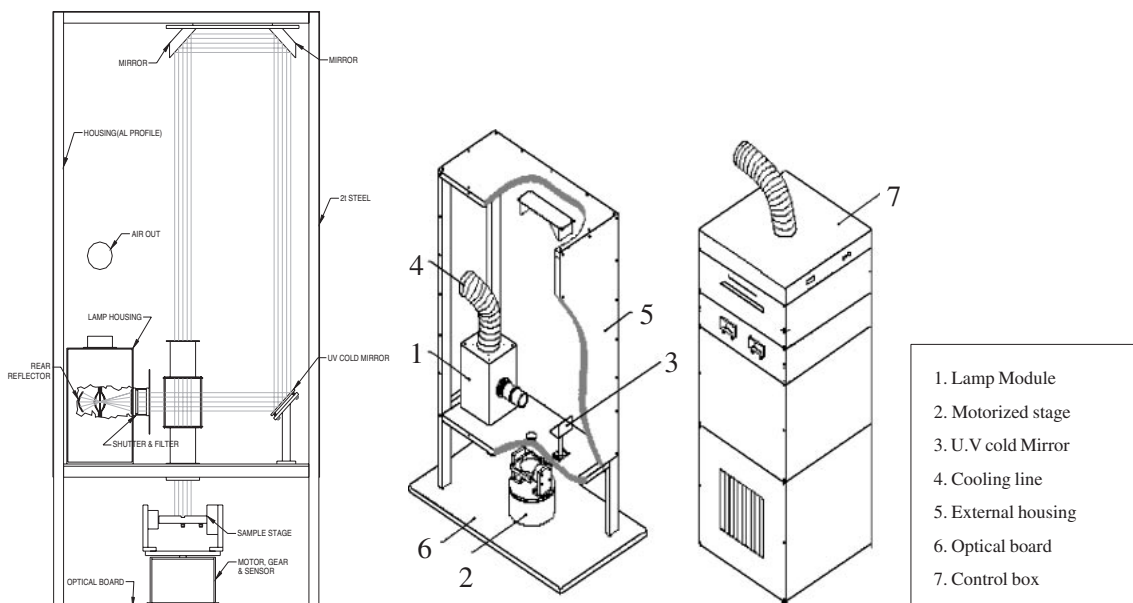


Fig. 3. Configuration of the MRPBI system.

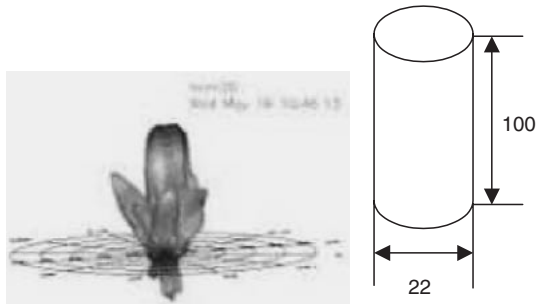


Fig. 5. Three-dimensional cylindrical MEMS antenna simulation using HFSS (high-frequency structure simulator).

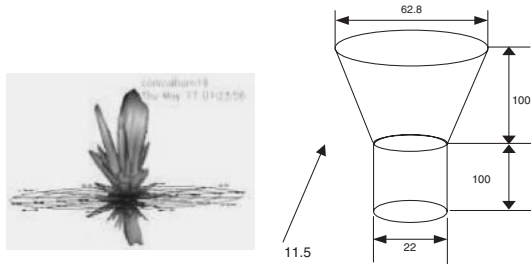


Fig. 6. Three-dimensional conical-horn MEMS antenna simulation using HFSS (high-frequency structure simulator).

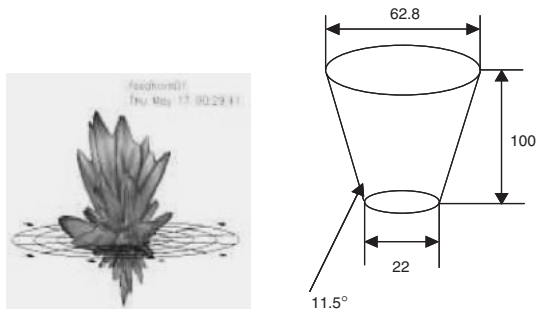


Fig. 7. 3D feed-horn MEMS antenna simulation using HFSS.

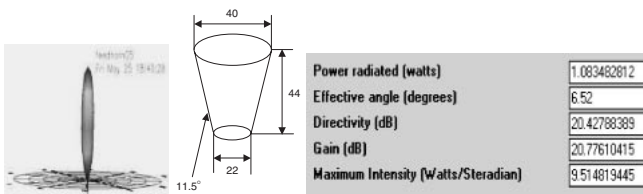


Fig. 8. Optimal design of a 3D feed-horn MEMS antenna using HFSS.

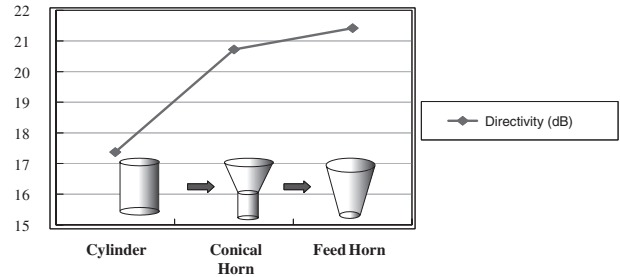


Fig. 9. Comparison of 3D MEMS antenna directivity.

that side lobes appear when the modeling parameters of the 3D MEMS antenna are not optimized. Figure 8 shows the optimal design parameters and the incident light radiation pattern obtained for the 3D feed-horn MEMS antenna using a high-frequency structure simulator (HFSS). The feed-horn angle parameter is  $11.5^\circ$ , and feed-horn diameter is  $22\ \mu\text{m}$ . The results indicated a directivity of  $20.42\ \text{dB}$  and a gain of  $20.77\ \text{dB}$ .

Table I shows a summary of the dependence of the gain of the 3D feed-horn MEMS antenna on its diameter and length obtained using HFSS. Figure 9 shows a comparison of the directivity gain of cylinder-, conical-horn- and feed-horn-shaped antennas. Among them, the directivity gain of the feed-horn-shaped antennas is the highest at  $22\ \text{dB}$ .

### 3.2 Design of microbolometer

The width of the absorption layer and length of the thermal isolation leg are very important factors in the design of a high-performance microbolometer. The absorption layer width of the microbolometer was matched to the horn diameter of the antenna in order to reduce coupling loss between the microbolometer and the antenna. The thermal

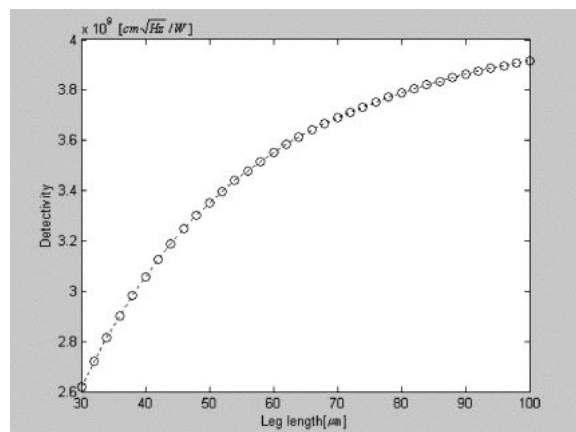


Fig. 10. Detectivity of microbolometer according to the leg length.

Table I. Simulated values for a 3D feed-horn MEMS antenna designed using HFSS.

Diameter ( $\mu\text{m}$ )	70	75	80	85	90	95
Length ( $\mu\text{m}$ )	145.23	169.35	195.05	224.48	251.58	282.35
Gain (dB)	16.83	18.76	19.40	17.36	12	14.43
Diameter ( $\mu\text{m}$ )	100	105	110	115	120	
Length ( $\mu\text{m}$ )	314.79	314.79	384.69	422.15	461.27	
Gain (dB)	13.82	13.50	10.05	9.51	12.31	

conductance  $G$ , heat capacitance  $C$  and thermal time constant of the microbolometer are  $3.94 \times 10^{-7}$  (W/K),  $4.39 \times 10^{-9}$  (J/K) and 11 ms, respectively, calculated using the following equations with the thermal isolation leg length of  $78.5 \mu\text{m}$ . Detectivity changes with leg length, as shown in Fig. 10. The theoretical detectivity was calculated as  $3.78 \times 10^9$  ( $\text{cm}\sqrt{\text{Hz}}/\text{W}$ ) using the following equations with the leg length of  $78.5 \mu\text{m}$ , considering only Johnson noise factor.

$$\begin{aligned} \text{Thermal conductance } G &= G_{\text{SiN}} + G_{\text{metal}} \\ &= K_{\text{SiN}}(W_{\text{SiN}}d_{\text{SiN}}/l) + K_{\text{metal}}(W_{\text{metal}}d_{\text{metal}}/l) \end{aligned}$$

Here,  $W_{\text{SiN}} = 5 \mu\text{m}$ ,  $d_{\text{SiN}} = 0.6 \mu\text{m}$ ,  $K_{\text{SiN}} = 0.045 \text{ W/cm}\cdot\text{K}$ ,  $W_{\text{metal}} = 3 \mu\text{m}$ ,  $d_{\text{metal}} = 0.2 \mu\text{m}$ ,  $K_{\text{metal}} = 0.29 \text{ W/cm}\cdot\text{K}$ .

$$\text{Thermal capacitance } C = \rho cV$$

Here, density  $\rho = 3.1 \text{ gm/cm}^3$ , specific heat capacity  $c = 3.33 \text{ J/cc}\cdot\text{K}$  and volume  $V = 0.6 \times \pi \times (30 \mu\text{m})^2$ .

$$\text{Thermal time constant } \tau = \frac{C}{G} = 11 \text{ ms}$$

$$\text{Detectivity } D^* = \frac{\alpha RI\eta}{G\sqrt{1 + \omega^2\tau^2}} \frac{\sqrt{A_d\Delta f}}{\sqrt{Vn^2}}$$

Here,  $\alpha$  is the TCR,  $R$  is the bolometer resistance,  $\eta$  is the absorption ratio,  $I$  is the bias current,  $\tau$ : thermal time constant,  $\omega = 2\pi \times 30 \text{ Hz}$ ,  $A_d$  is the absorption layer area,  $\sqrt{Vn^2}/\sqrt{\Delta f} \cong \sqrt{4kTR}$  is Johnson noise.

### 3.3 Characteristics of performance

We verified the performance of the antenna-coupled microbolometer by comparing with a conventional microbolometer. We characterized three types of microbolometers, namely, the small-area microbolometer, antenna-coupled microbolometer and large-area microbolometer. Figure 11 shows a comparison of the three types of microbolometer. The small-area microbolometer first one has a low heat capacity so it has a fast response time. The antenna-coupled microbolometer second one has a low heat capacity and a fast response time, but it has a large detecting area so it enhances the absorption performance. The large-area microbolometer third one has a large detecting area, but

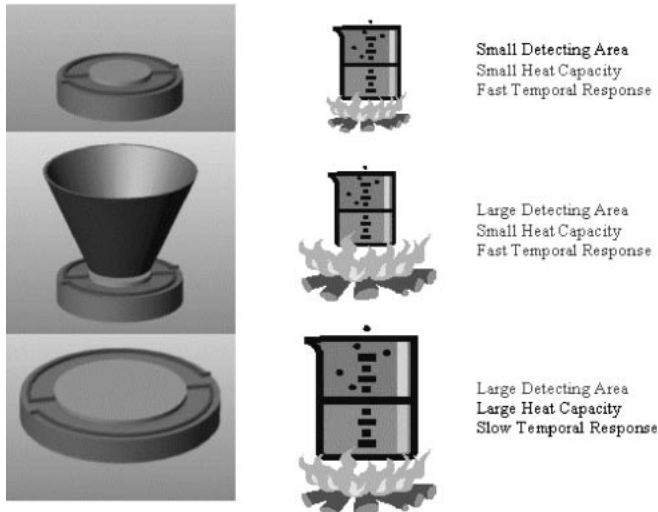


Fig. 11. Three different types of microbolometers.

its heat capacity is large so it has a slow response time. The above result shows that the antenna-coupled microbolometer has better properties than the other microbolometers. Next, we compared the performances of the three types of microbolometers quantitatively with respect to the detectivity of the antenna-coupled microbolometer  $D_A^*$ , the detectivity of the large-area microbolometer  $D'^*$  and the detectivity of the small-area microbolometer  $D^*$ . We also analyzed the detectivity under the three different noise conditions. First, when noise is independent of microbolometer area, then the detectivity of each microbolometer is expressed using the following equations if one assumes that the area ratio  $A_A/A_d = 4$  and the antenna directivity = 100 (20 dB). Here,  $w$  is the modulation frequency,  $H$  is the heat capacity and  $K$  is the heat conductivity.

$$\begin{aligned} D_A^* : D'^* : D^* &= \begin{cases} \eta_A \sqrt{\frac{A_A}{A_d}} : \sqrt{\frac{A_A}{A_d}} : 1 \\ \eta_A \sqrt{\frac{A_A}{A_d}} : \sqrt{\frac{A_d}{A_A}} : 1 \end{cases} \\ &= \begin{cases} 2 : 2 : 1 & \left( \frac{\omega^2 H^2}{K_{\text{eff}}^2} \ll 1 \right) \\ 2 : 0.5 : 1 & \left( \frac{\omega^2 H^2}{K_{\text{eff}}^2} \gg 1 \right) \end{cases} \end{aligned}$$

Second, when the dominant noise is the background noise, which is a case of background limited-infrared performance (BLIP). In the BLIP case, the detectivity can be expressed using the following the equations.

$$\begin{aligned} D_A^* : D'^* : D^* &= \begin{cases} \sqrt{\frac{\eta_A D_0}{2}} : 1 : 1 \\ \sqrt{\frac{\eta_A D_0}{2}} : \frac{A_d}{A_A} : 1 \end{cases} \\ &= \begin{cases} 7.1 : 1 : 1 & \left( \frac{\omega^2 H^2}{K_{\text{eff}}^2} \ll 1 \right) \\ 7.1 : 0.25 : 1 & \left( \frac{\omega^2 H^2}{K_{\text{eff}}^2} \gg 1 \right) \end{cases} \end{aligned}$$

Third, when principle noise is a scattered light source, then the detectivity is expressed using the following equations.

$$\begin{aligned} D_A^* : D'^* : D^* &= \begin{cases} \frac{D_0}{2} \sqrt{\frac{A_d}{A_A}} : \sqrt{\frac{A_d}{A_A}} : 1 \\ \frac{D_0}{2} \sqrt{\frac{A_d}{A_A}} : \sqrt{\left(\frac{A_d}{A_A}\right)^3} : 1 \end{cases} \\ &= \begin{cases} 25 : 0.5 : 1 & \left( \frac{\omega^2 H^2}{K_{\text{eff}}^2} \ll 1 \right) \\ 22 : 0.125 : 1 & \left( \frac{\omega^2 H^2}{K_{\text{eff}}^2} \gg 1 \right) \end{cases} \end{aligned}$$

On the basis of the above result, the antenna-coupled microbolometer has a better performance than the other microbolometers. In particular, when scattered light is the dominant noise source, the detectivity of the antenna-coupled microbolometer is increased to approximately 25

Table II. Summary of detectivity comparisons for three different microbolometer types under three different noise conditions.

Condition (Principle Noise)	Small-Area Bolometer	Antenna-Coupled Bolometer	Large Area Bolometer
Area independent	1	2	0.5–2
Detectivity BLIP	1	7	0.25–1
Scattered IR	1	25	0.125–0.5

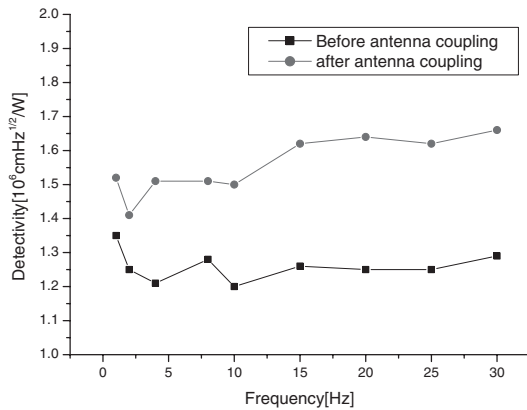


Fig. 12. Enhanced detectivity of 3D MEMS antenna-coupled microbolometer.

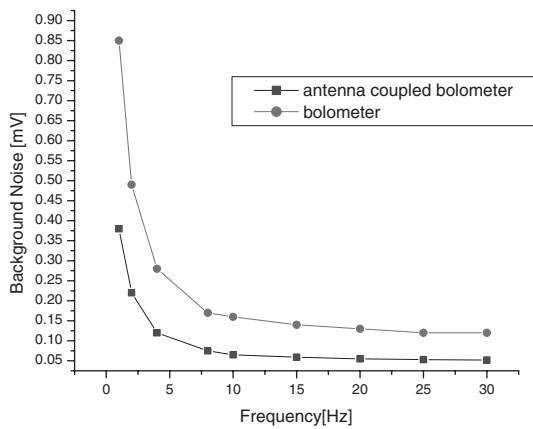


Fig. 13. Reduced background noise of 3D MEMS antenna-coupled microbolometer.

times that of the conventional microbolometer. Table II summarizes the detectivity of the three different types of microbolometers under the three different noise conditions. From the performance characterization of the antenna-coupled microbolometer, we confirmed that the antenna-coupled microbolometer has a high detectivity and reduced background noise, as shown in Figs. 12 and 13. The antenna directivity was measured by changing the blackbody source radiation direction. Figure 14 shows that the output signal changed as a function of incident beam angle.

#### 4. Experiments and Results

##### 4.1 Fabrication of feed-horn mold array

We used two methods of fabricating the 3D feed-horn-

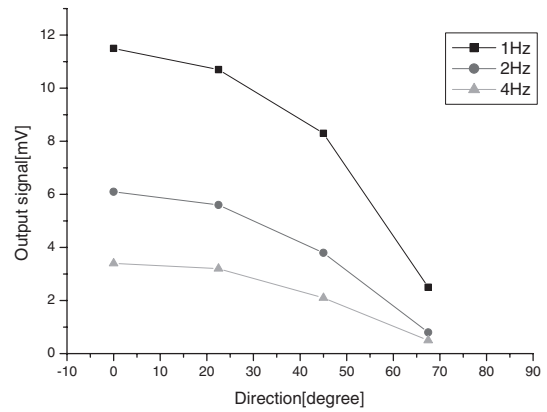


Fig. 14. Experimental results of the dependence of output signal on incident beam angle.

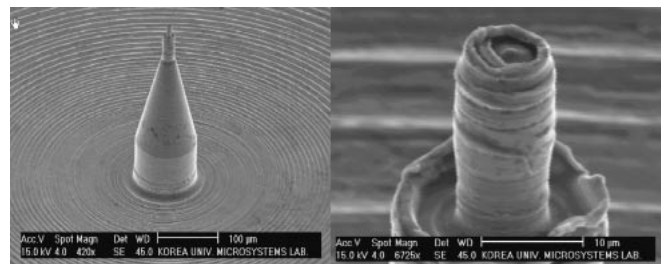


Fig. 15. SEM images of conventional machining results for a 3D antenna mold structure.

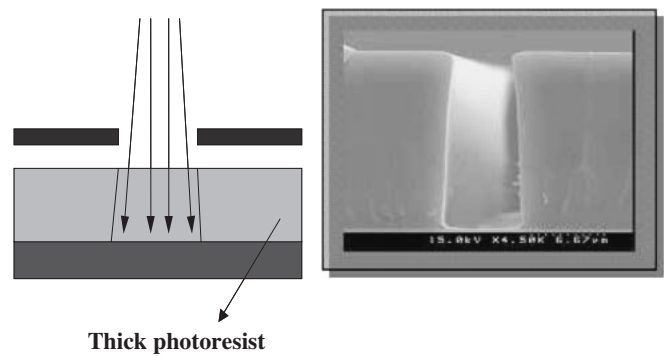


Fig. 16. SEM image and schematic drawing of negative photoresist PMER photolithography experiment using a conventional UV photolithography apparatus.

shaped mold structure array. Figure 15 shows the SEM images of 3D antenna molds fabricated by conventional precision machining. These experimental results show a rough surface. Figure 16 shows the results of a negative photoresist PMER experiment using a conventional UV lithography apparatus. These results indicate that it is very difficult to obtain a high-aspect-ratio structure using this kind of conventional lithography.

Figure 17 shows a vertical sidewall structure array, which is over 100  $\mu\text{m}$  high and which was fabricated using a negative photoresist, PMER, and a MRPBI system. The fabrication steps for the high vertical sidewall are 2-step spin coating (500 rpm/s, 600 rpm/s) for a stabilization condition

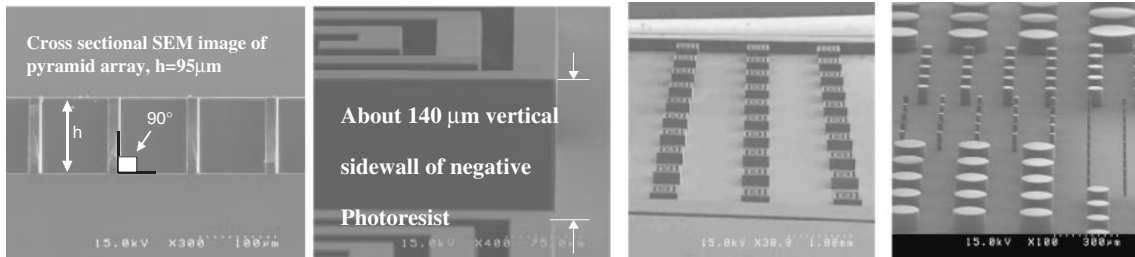


Fig. 17. SEM images of a vertical sidewall array using a negative photoresist PMER, fabricated using the MRPBI system.

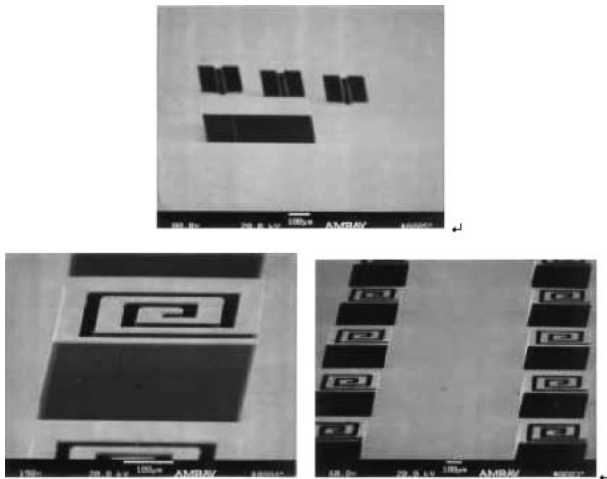


Fig. 18. SEM images of an inclined sidewall array using negative photoresist SU-8 fabricated using the MRPBI system.

of 5 min, prebaking at 110°C for 25 min, post exposure bake (PEB) at 100°C/15 min and exposure for 1800 s. When exposure time is over 2400 s, a very strong hard reflective coating is obtained and it becomes very difficult to obtain a vertical sidewall. The inclined sidewall array fabricated using the negative SU-8 photoresist and the MRPBI system is shown in Fig. 18. The SEM images in Figs. 19(a) and 19(b) show quadruple shape arrays, while Figs. 19(c) and 19(d) show teapot-shaped arrays with serious hard reflections. The experimental parameters are a 20°-tilted stage with the y-axis direction rotated 360° and an exposure time of 1800 s. The exposure time is the most important factor in this experiment.

Figure 20 shows a schematic drawing of the 3D feed-

horn-shaped array fabricated by UV exposure while rotating the tilted substrate. We fabricated the 3D feed-horn-shaped mold array using a negative photoresist in the MRPBI system. The optimal fabrication step for making a 3D feed-horn-shaped mold array is 2-step spin coating (500 rpm/s, 1600 rpm/s) under a stabilization condition of 6 min, with prebaking at 110°C/25 min and post exposure baking at 100°C/15 min; Figures 21(a), 21(b), and 21(c) are for 35°, 30°- and 25°-tilted stages, respectively. The exposure time was 250 s. In this experiment, it was necessary to control the 3D feed-horn antenna angle, hence, several experiments with mold structure at various angles were performed by controlling the x-y-z stage and protecting it against UV reflection with a bottom antireflection coating (BARC). Figures 21(d), 21(e), and 21(f) show a 3D feed-horn-shaped mold arrays.<sup>8,9)</sup>

#### 4.2 Fabrication of an antenna plate using micromolding in capillaries by polydimethylsiloxane

The 3D MEMS antenna plate was fabricated using polydimethylsiloxane (PDMS) and the application of the MMIC technique. Micromolding in capillaries represents another non-photolithographic method of forming a complex

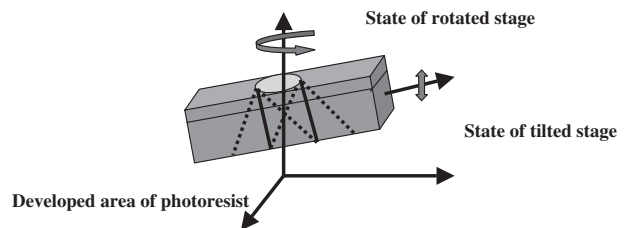


Fig. 20. Schematic drawing of 3D feed-horn mold fabrication.

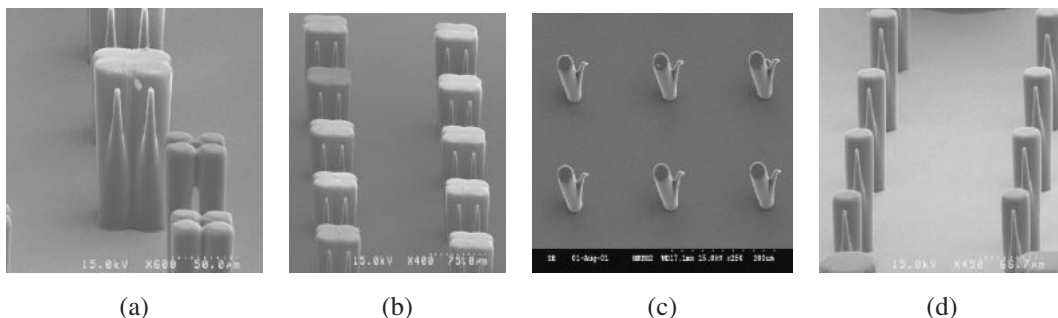


Fig. 19. (a) and (b) SEM images of quadruple shape arrays, and (c) and (d) SEM images of teapot-shaped arrays using negative PMER photoresist fabricated using the MRPBI system.

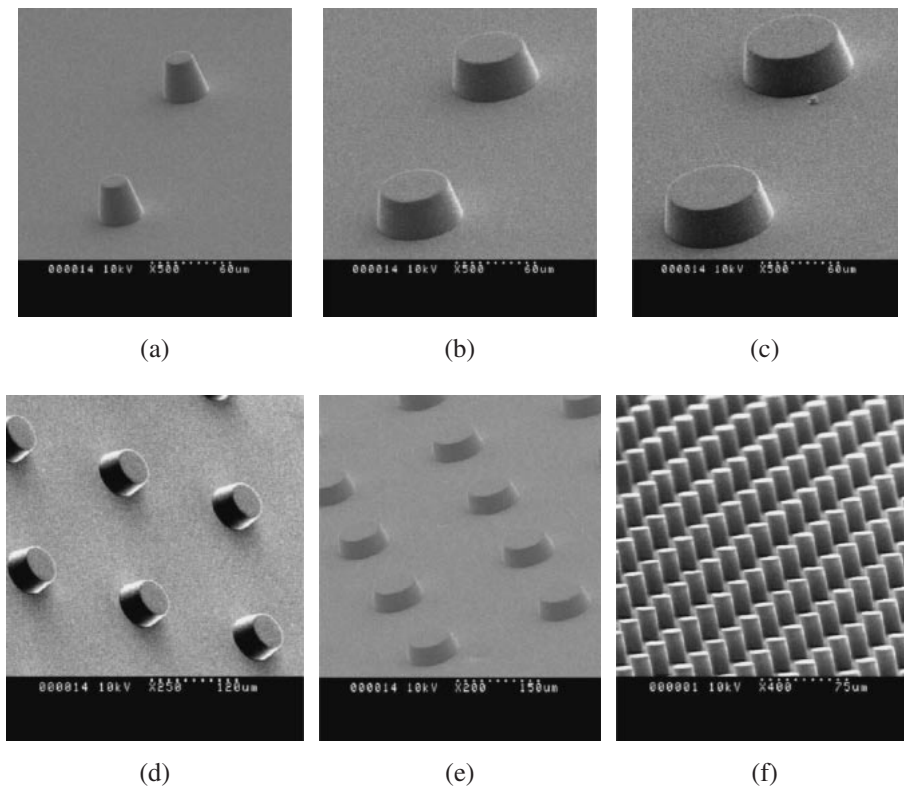


Fig. 21. SEM images of feed-horn-shaped molds made of a negative photoresist PMER fabricated using the MRPBI system.

microstructure on both planar and curved surfaces.

Capillary filling is a very simple and well-known phenomenon and the dynamics of the wetting and spreading of liquids in capillaries has been studied systematically. The flow of a liquid in a capillary occurs because of a pressure difference between two hydraulically connected regions of the liquid mass, and the direction of flow decreases this difference in pressure. A curing agent and polydimethylsiloxane (PDMS) prepolymer (SYLGARD 184 Silicone Elastomer Kit Dow Corning, Midland, Michigan, USA) were thoroughly mixed in a 1 : 10 weight ratio.

The PDMS mixture was injected into the master, and then a weight plate was placed over the back surface of the substrate. The clamped PDMS was cured for 1 h at 65°C in an oven. After curing, the thin PDMS antenna plate was peeled off the master and plastic plate. Figure 22 shows the setup for MMIC using PDMS. After fabricating the antenna plate, its inner metal coating was formed through a mechanism in which metal coating layers, namely 500 Å

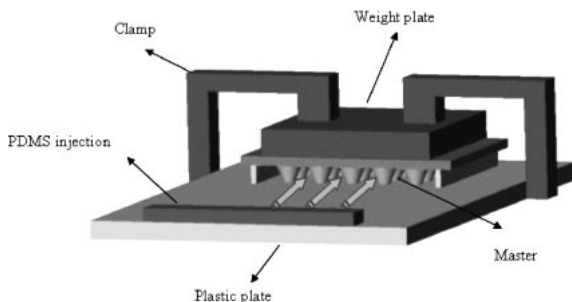


Fig. 22. Fabrication of antenna plate using polydimethylsiloxane (PDMS) injection by micro molding in capillaries (MIMIC).

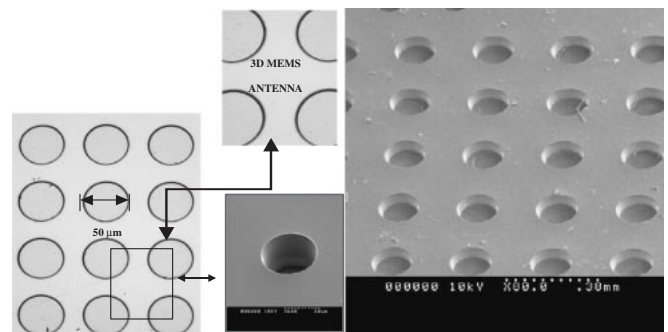


Fig. 23. SEM images of 3D MEMS antenna.

Ti and 2000 Å Au, were deposited using a simultaneously rotated y-axis and z-axis e-gun evaporator. The key element of the technique is the selection of the bottom substrate because PDMS material is easily stretched, so it is fabricated with a diameter larger than that of master. Figure 23 shows a microscopy image of the 3D MEMS antenna and a SEM image of the 3D feed-horn antenna plate.

#### 4.3 Microassembly using mesh structure bonding (MSB)

The microassembly of 3D MEMS antenna arrays and microbolometer arrays is difficult using the conventional MEMS bonding process. Therefore of 2.5 μm IR detector arrays were floated on the substrate, and the thickness of the bonding material required for optimization of contact gap is below 2.5 μm. All of the IR detector arrays were bonded with the 3D MEMS antenna in the low-temperature process. To overcome these limitations, the proposed novel 3D MEMS bonding technique is mesh structure bonding (MSB)

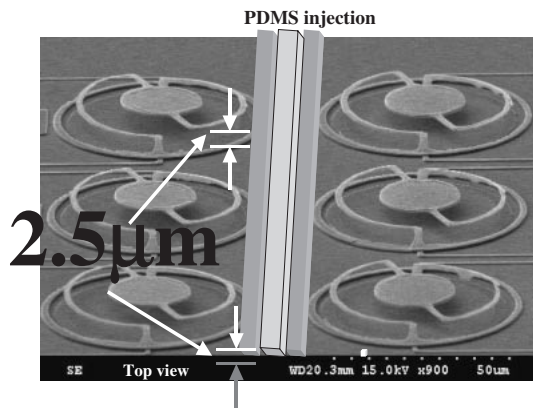


Fig. 24. Mesh structure bonding (MSB) using microchannels with PDMS.

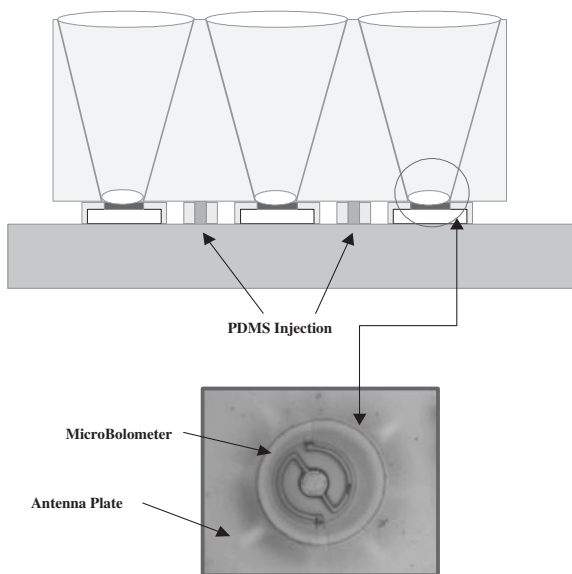


Fig. 25. Microassembly for 3D MEMS antenna with microbolometer using mesh structure bonding (MSB) technique.

using microchannels. This MSB technique can be used to induce low-temperature bonding, control the bonding material thickness and realize precision bonding of the mesh

structure. Figures 24 and 25 show method of mesh structure bonding (MSB) using microchannels with PDMS injection and the experiment results of microassemblies for the 3D MEMS antenna with an IR detector using the mesh structure bonding (MSB) technique, respectively.

### 5. Conclusion

In this paper, we have described novel techniques and methods for fabricating a 3D feed-horn MEMS antenna using a new UV lithography apparatus called the mirror-reflected parallel-beam illuminator (MRPBI) system and proposed a microbolometer coupled with a 3D feed-horn antenna. The optimal size of the antenna and the microbolometer are designed for enhancing the detectivity of the device. We fabricated the microbolometer using the surface micromachining method and also proposed a new bonding method using PDMS as a bonding material. From the performance characterization of the antenna-coupled microbolometer, we confirmed that the antenna-coupled microbolometer has a high detectivity.

### Acknowledgements

The authors wish to acknowledge that this paper is the result of research accomplished with the financial support of the Intelligent Microsystems Center, Seoul, Korea, which is carrying out one of the 21st New Frontier R&D Projects sponsored by the Korean Ministry of Science & Technology.

- 1) R. A. Wood: Proc. SPIE **2020** (1993) 322.
- 2) P. L. Marasco and E. L. Dereniak: Proc. SPIE **2020** (1993) 363.
- 3) H. Jerominek, T. D. Pope, C. Alain and R. Zhang: Proc. SPIE **3436** (1998) 585.
- 4) M. Razeghi *et al.*: J. Kor. Phys. Soc. **39** (2000) S257.
- 5) J. Y. Park, K. T. Kim, H. J. Shin, S. Moon and J. J. Pak: J. Kor. Phys. Soc. **41** (2002) 552.
- 6) A. Rogalski: *Infrared Detector* (Golden and Breach Science Publishers, Boston, 2000).
- 7) B. E. Cole, R. E. Higashi and R. A. Wood: Proc. IEEE **86** (1998) 1211.
- 8) E. L. Dereniak: *Infrared Detectors and Systems* (John Wiley & Sons, New York, 1995).
- 9) L. F. Tompson: *Introduction to Microlithography* (John Wiley & Sons, New York, 1999) 2nd ed.